MATERIALS SCIENCE

# Multi-heterointerfaces for selective and efficient urea production

Danyan Zhang[1,3], Yurui Xue[1,2,*], Xuchen Zheng[1,3], Chao Zhang[1,3] and Yuliang Li[1,2,3,*]

## ABSTRACT

A major impediment to industrial urea synthesis is the lack of catalysts with high selectivity and activity, which inhibits the efficient industrial production of urea. Here, we report a new catalyst system suitable for the highly selective synthesis of industrial urea by *in situ* growth of graphdiyne on the surface of cobalt–nickel mixed oxides. Such a catalyst is a multi-heterojunction interfacial structure resulting in the obvious incomplete charge-transfer phenomenon between a graphdiyne and metal oxide interface and multiple intermolecular interactions. These intrinsic characteristics are the origin of the high performance of the catalyst. Studies on the mechanism reveal that the catalyst could effectively optimize the adsorption/desorption capacities of the intermediate and promote direct C–N coupling by significantly suppressing by-product reactions toward the formation of $H_2$, CO, $N_2$ and $NH_3$. The catalyst can selectively synthesize urea directly from nitrite and carbon dioxide in water at room temperature and pressure, and exhibits a record-high Faradaic efficiency of 64.3%, nitrogen selectivity ($N_{urea}$-selectivity) of 86.0%, carbon selectivity ($C_{urea}$-selectivity) of ∼100%, as well as urea yield rates of 913.2 $\mu$g h$^{-1}$ mg$_{cat}$$^{-1}$ and remarkable long-term stability.

**Keywords:** porous materials, carbon materials, multi-heterointerfaces, urea synthesis, high-performance conversion

[1]Institute of Chemistry, Chinese Academy of Sciences, Beijing 100190, China; [2]Shandong Provincial Key Laboratory for Science of Material Creation and Energy Conversion, Science Center for Material Creation and Energy Conversion, School of Chemistry and Chemical Engineering, Shandong University, Jinan 250100, China and [3]University of Chinese Academy of Sciences, Beijing 100049, China

*Corresponding authors. E-mails: yrxue@sdu.edu.cn; ylli@iccas.ac.cn

## INTRODUCTION

Urea $[CO(NH_2)_2]$ has always influenced the development of industry and agriculture in the world because of its important position in the agriculture and chemical industry [1,2]. The development of efficient urea production is of great significance for increasing crop production to meet the demands of a growing population and basic industrial raw materials [3,4]. However, current industrial urea production is mainly achieved by (i) reacting liquid ammonia ($NH_3$) with liquid carbon dioxide ($CO_2$) to form ammonium carbamate ($NH_2COONH_4$) and (ii) the decomposition of $NH_2COONH_4$ to obtain urea and water at high temperatures and pressures consuming large amounts of fossil fuels [5–7]. In addition, the raw material $NH_3$ is produced by a hashing, energy-intensive, complex Haber–Bosch process [8,9]. In order to alleviate the problem of energy shortage and achieve the goal of carbon neutrality, exploring catalyst innovation development is a new path for the sustainable development of the world economy in the future [10–13].

Electrochemical coupling of $N_2$ and $CO_2$ in water for urea synthesis is an attractive approach [14,15]. However, the high activation energy barrier of N≡N and the limited solubility of $N_2$ in water lead to a low urea yield rate ($Y_{urea}$) and low Faradaic efficiency (FE) [16–18]. In view of this, exploration of the coupling of $NO_2^-$ with $CO_2$ in water with high solubility and a low activation energy barrier may provide a renewable and economically promising route for urea production under ambient conditions [19,20]. As expected, achieving high FE and nitrogen atomic efficiency (NE) in urea simultaneously is very desirable, but this is an acknowledged scientific challenge that must be overcome by the following factors: how to control the competition of the parallel $CO_2$ and/or $NO_2^-$ reduction and hydrogen evolution reactions resulting in low FE, how to improve the low selectivity for the C–N coupling and

how to improve the selectivity to form intermediates of reaction.

Catalysts with multi-heterointerface structures generally show higher selectivity and activity in catalysis than single-component ones due to the improved electron transferability, the unevenly distributed interface charge on the surface of the catalysts, the increased number of active sites and the optimized adsorption/desorption behaviors of the reactants/intermediates [21–25]. A key strategy for building such an interface is the perfect combination of multicomponent nanoparticles (e.g. metal oxides, hydroxides or metal alloys) as acceptor units with supporting materials as donor units [26–28]. Such catalysts greatly improve the selectivity, activity and stability compared with single-component ones, due to high-density charge transfer between donors and receptors [29–31]. This provides a solid foundation for our rational design of high-performance multi-interface catalysts.

Graphdiyne (GDY), a rising star on the horizon of carbon materials comprising sp/sp²-cohybridized carbon atoms, has established a solid position in the fields of electrocatalysis, photocatalysis, energy conversion, etc. [32–35] due to its fascinating and unique advantages such as the uneven surface charge distribution, infinite natural pores, highly $\pi$-conjugated structure, excellent stability, etc. Notably, GDY is the only all-carbon material that can be grown in arbitrary materials, which allows the controlled synthesis of ideal interface structures with determined valence states and accurate chemical structures [36–38]. Besides, the unique incomplete charge-transfer ability of GDY-based catalysts endows the catalysts with ultra-high catalytic selectivity and activity for various reactions [39,40].

In this study, selective and efficient urea production was achieved on a multi-heterojunctions interfacial structure of Co–NiO$_x$@GDY. Experimental results show that the unique structures of the catalyst can result in the strong incomplete charge-transfer phenomenon between the GDY and metal oxide interface and multiple intermolecular interactions, leading to high electrocatalytic performances. Studies on the mechanism show that Co–NiO$_x$@GDY can simultaneously optimize the $CO_2/CO$ adsorption ability and promote the $NH_3$ formation, which is expected to provide large abundant $_*CO$ intermediates and $NH_2$-related intermediates for the direct C–N coupling accompanied by the significant suppression of the by-product reactions toward the formation of $H_2$, CO, $N_2$ and $NH_3$. Benefitting from these unique features, Co–NiO$_x$@GDY with multi-heterointerfaces reaches a record-high FE of 64.3%, N$_{urea}$-selectivity of 86.0%, C$_{urea}$-selectivity of ∼100%, as well as urea yield rates

of 913.2 $\mu$g h$^{-1}$ mg$_{cat}$$^{-1}$ and remarkable long-term stability.

## RESULTS AND DISCUSSION

Figure 1 illustrates the synthesis route for the controlled synthesis of Co–NiO$_x$@GDY through a three-step strategy including the first growth of a film of cobalt–nickel bimetal mixed layered double hydroxide nanosheets on the surface of nickel foam (Co–NiO$_x$H$_y$) via an electrodeposition method, followed by a calcination treatment of the as-prepared Co–NiO$_x$H$_y$ at 300°C for 2 h during which the porous Co–NiO$_x$ nanosheets were obtained, and finally the *in situ* growth of ultra-thin GDY films on the surface of Co–NiO$_x$ through a cross-coupling reaction with hexaethynylbenzene (HEB) as the precursor (please see the Experimental Section for more details).

The models in Fig. 2a illustrate the morphology changes of the samples from nanosheets with smooth surfaces to porous ones and finally to multilayered 2D nanosheets. As shown in Fig. 2b and c, a film of Co–NiO$_x$H$_y$ nanosheets with a wrinkled surface was vertically aligned and ordered grown on the surface of the substrates. A 3D porous electrode with uniform element distribution was then obtained (Supplementary Fig. S1). Such architectures benefit from the increase in the surface area and the number of active sites of the samples. After the calcination treatment, the Co–NiO$_x$ nanosheets collapsed and became more porous due to the dehydration of the precursors at high temperatures (Fig. 2e and f, and Supplementary Fig. S2), resulting in a larger specific surface area (SSA) of 4.68 m² g$^{-1}$ (Fig. 2g) than the Co–NiO$_x$H$_y$ sample (Fig. 2d). By using Co–NiO$_x$ nanosheets as the substrate, the GDY nanosheets were further *in situ* grown on the surface of the Co–NiO$_x$ nanosheets (Fig. 2h and i), leading to the formation of a vertically aligned and densely interconnected ordered 3D electrode. Figure 2k shows the uniform distribution of Co, Ni, O and C elements for the Co–NiO$_x$@GDY sample, revealing the successful growth of GDY. The absence of a Cu signal in the total spectrum of the elemental distribution surface (Supplementary Fig. S3) proves that our synthesized material does not contain Cu elements and successfully avoids the interference of Cu elements in the catalytic reaction.

The mesoporous nature of the prepared materials was then identified from the nitrogen adsorption–desorption isotherm at 77 K. Co–NiO$_x$H$_y$ (Fig. 2d) and Co–NiO$_x$ (Fig. 2g) samples show Type IV isotherms with an H$_3$-type hysteresis loop [41,42], which indicates the presence of a mesoporous
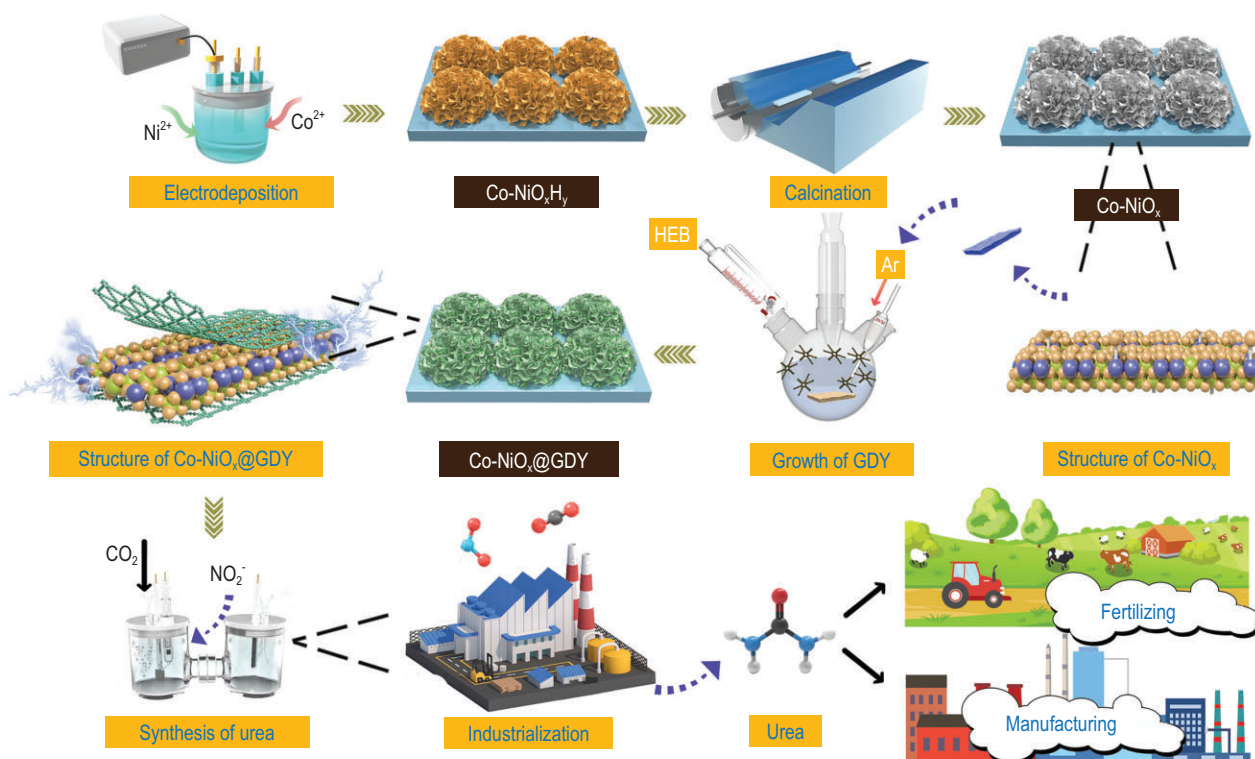
**Figure 1.** Schematic representation of the synthesis routes of Co–NiO$_x$@GDY.

structure with mesopores predominantly lying between 5–7 and 8–10 nm, respectively. Co–NiO$_x$@GDY has an H$_4$-type hysteresis loop with a more pronounced hysteresis loop (Fig. 2j). Correspondingly, the pores in Co–NiO$_x$@GDY show smaller sizes concentrated at 4 nm than Co–NiO$_x$H$_y$ (Fig. 2d) and Co–NiO$_x$ (Fig. 2g). As expected, Brunauer–Emmett–Teller results show that Co–NiO$_x$@GDY has the largest SSA of 13.70 m$^2$ g$^{-1}$ compared with the Co–NiO$_x$H$_y$ and Co–NiO$_x$ samples, indicating the presence of more active sites in the presence of GDY. Co–NiO$_x$@GDY also shows a much higher CO$_2$ uptake ability (3.86 cm$^3$ g$^{-1}$) at 298 K than pure Co–NiO$_x$ (1.93 cm$^3$ g$^{-1}$), indicating the greatly enhanced CO$_2$ affinity after the introduction of GDY. XRD patterns for Co–NiO$_x$ (Fig. 2m) show two diffraction peaks at 36.61° and 44.54° corresponding to the (311) and (400) crystal planes of NiCo$_2$O$_4$, one diffraction peak at 42.8° corresponding to the (100) crystal plane of NiCoO$_2$, the peak at 62.85° corresponding to the (110) crystal plane of NiO and the peak at 51.2° corresponding to the (100) crystal of Co, respectively [43]. After the *in situ* growth of GDY, the intensity of the metal peaks decreased and new peaks (at 25.42° and 43.14°) corresponding to the carbon materials (GDY) were observed, which indicates the successful incorporation of GDY and Co–NiO$_x$ species.

Transmission electron microscopy (TEM) images show the presence of Ni(OH)$_2$ (300), Co(OH)$_2$ (101) in Co–NiO$_x$H$_y$ nanosheets (Supplementary Fig. S4). Dark-field TEM (DF-TEM) is a high-throughput and diffraction-sensitive imaging technique, which can directly image crystal symmetry by selecting an inner diffraction spot with a selected aperture in the diffraction pattern [44–47]. We use selected-area electron diffraction and DF-TEM to characterize the crystal structure of our catalysts. The bright-field image and diffraction pattern (Supplementary Fig. S5) reveal that Co–NiO$_x$H$_y$ contains several grains with different orientations. Figure 3a and b shows the corresponding DF-TEM images from two different areas with different selected spots in the diffraction pattern. Obviously, the hydroxide Co–NiO$_x$H$_y$ obtained by direct electrodeposition with poor crystallinity results in poor visualization of the directional diffraction. The high-resolution TEM (HRTEM) images of Co–NiO$_x$H$_y$ (Fig. 3c and d) show nanosized crystallites with various orientations, including the (300) plane of Ni(OH)$_2$ with a lattice constant of 0.155 nm and the (101) plane of Co(OH)$_2$ with a lattice constant of 0.237 nm, match well with the XRD results (Supplementary Fig. S6). After calcination, the Co–NiO$_x$ nanoarrays are porous with a
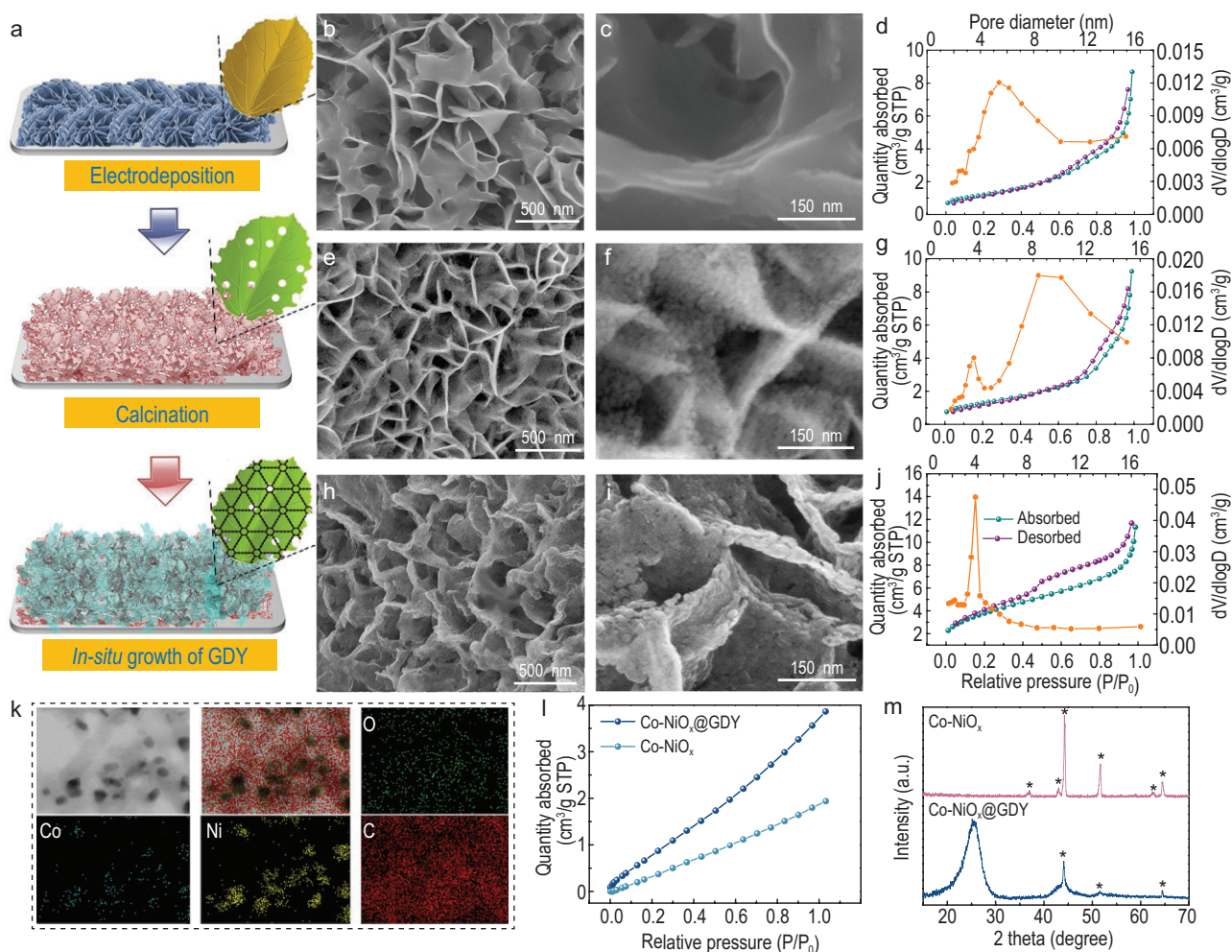
**Figure 2.** (a) Model diagram of the catalysts. (b) Low- and (c) high-magnification SEM images of Co–NiO$_x$H$_y$. (d) The N$_2$ adsorption/desorption isotherms and pore-size distributions of Co–NiO$_x$H$_y$. (e) Low- and (f) high-magnification SEM images of Co–NiO$_x$. (g) The N$_2$ adsorption/desorption isotherms and pore-size distributions of Co–NiO$_x$. (h) Low- and (i) high-magnification SEM images of Co–NiO$_x$@GDY. (j) The N$_2$ adsorption/desorption isotherms and pore-size distributions of Co–NiO$_x$@GDY. (k) The STEM and elemental mapping images of Co, Ni, C and O in the Co–NiO$_x$@GDY. (l) The CO$_2$ adsorption isotherms comparison of Co–NiO$_x$ and Co–NiO$_x$@GDY. (m) Powder XRD patterns of Co–NiO$_x$ and Co–NiO$_x$@GDY.

more rigid and tighter structure (Supplementary Fig. S7a and b).

The bright-field image and diffraction pattern of the as-prepared Co–NiO$_x$ revealed the polymorphism of the Co–NiO$_x$ (Supplementary Fig. S8). DF-TEM images in Fig. 3e and f reveal that the samples are constituted by the NiO (110) facets and Co–NiO$_x$ (400) and (311) facets, respectively, accompanied by numbers of grain boundaries that might lead to the formation of new active sites. When overlaying the two dark-field images, we marked the highlighted area in the NiO (110) dark-field image as yellow and the Co–NiO$_x$ (400), (311) dark-field image as red. In the superimposed dark-field images, we found that the yellow area and the red area show no overlaps but only one kind of grain appears in the same position, which proves that Co–NiO$_x$ is multiphased. For a deeper understanding of the

Co–NiO$_x$ grains, the HRTEM images in Fig. 3g and h depict mainly nanosized grains with three different orientations. We identified diverse geometries for individual grains and the (110) plane of NiO; the (311) and (400) planes can be clearly observed with lattice constants of 0.148, 0.242 and 0.203 nm, respectively. Co–NiO$_x$ contains a high density of grain interfaces, which causes the distortion of the atomic layers at the interface (Supplementary Fig. S9) and a high density of dislocations and steps, which are helpful to expose additional catalytic sites and improve the catalytic performance [48]. Such a unique grain boundary enriched structure is well preserved after the *in situ* growth of GDY nanosheets in the TEM images of Co–NiO$_x$@GDY (Supplementary Fig. S10a and b) in which some tiny crystallite fragments have coalesced to form larger ones. Supplementary Fig. S11 shows the bright-field
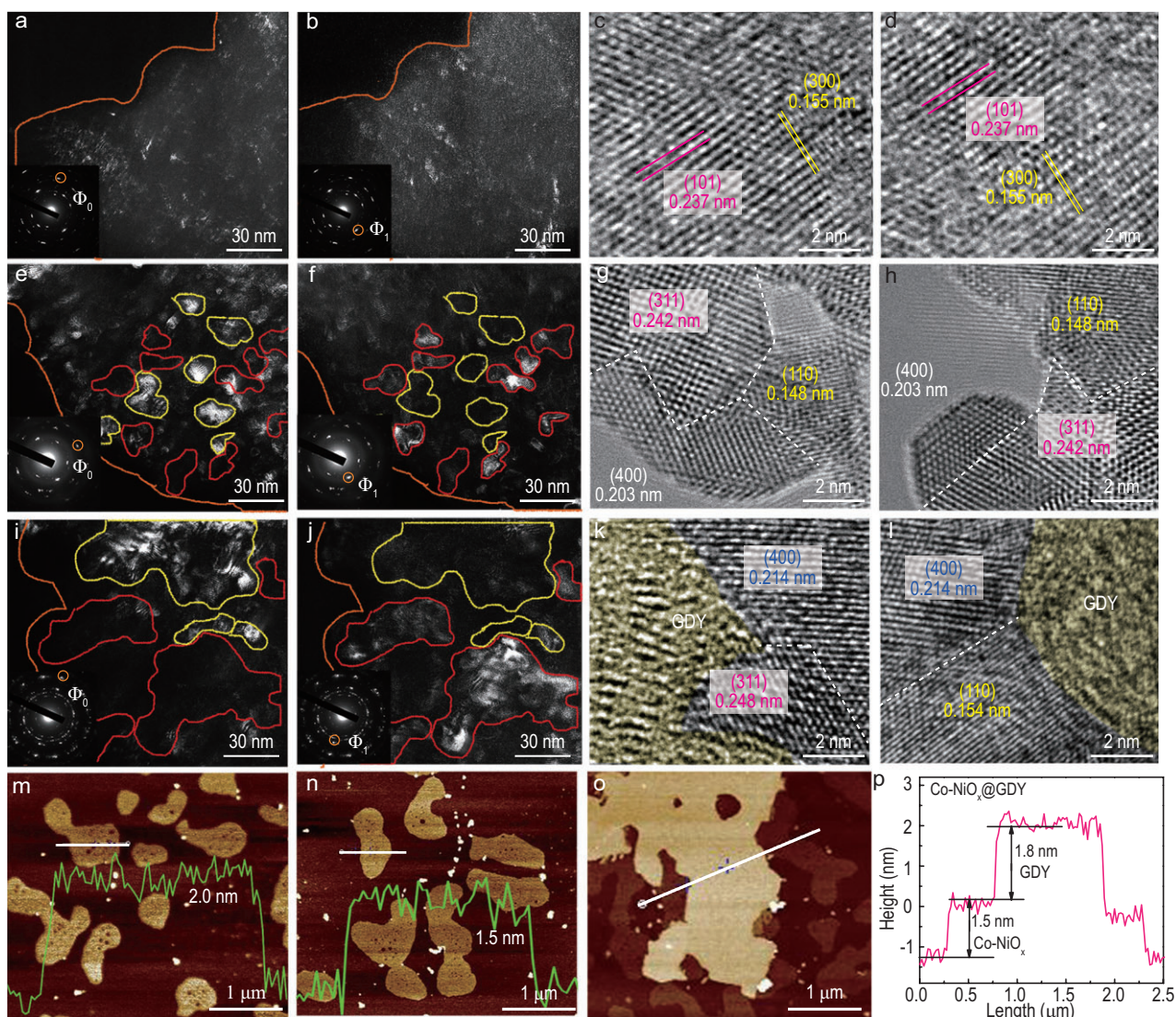
**Figure 3.** (a) DF-TEM images of Co–NiO$_x$H$_y$, obtained by selecting the inner diffraction spots $\Phi_0$ [corresponding to Ni(OH)$_2$ (300) crystal diffraction lattice]. (b) DF-TEM images of Co–NiO$_x$H$_y$, obtained by selecting the inner diffraction spots $\Phi_1$ [corresponding to Co(OH)$_2$ (101) crystal diffraction lattice]. (c and d) The HR-TEM images of Co–NiO$_x$H$_y$. (e) DF-TEM images of Co–NiO$_x$, obtained by selecting the inner diffraction spots $\Phi_0$ [corresponding to NiO (110) crystal diffraction lattice]. (f) DF-TEM images of Co–NiO$_x$, obtained by selecting the inner diffraction spots $\Phi_1$ [corresponding to Co–NiO$_x$ (400), (311) crystal diffraction lattice]. (g and h) The HRTEM images of Co–NiO$_x$. (i) DF-TEM images of Co–NiO$_x$, obtained by selecting the inner diffraction spots $\Phi_0$ [corresponding to NiO (110) crystal diffraction lattice]. (j) DF-TEM images of Co–NiO$_x$, obtained by selecting the inner diffraction spots $\Phi_1$ [corresponding to Co–NiO$_x$ (400), (311) crystal diffraction lattice]. (k and l) The HRTEM images of Co–NiO$_x$@GDY. The AFM images and thickness measurement of (m) Co–NiO$_x$H$_y$, (n) Co–NiO$_x$ and (o and p) Co–NiO$_x$@GDY.

image and diffraction pattern of the as-prepared Co–NiO$_x$@GDY. The larger highlighted regions in DF-TEM images (Fig. 3i and j) indicate that some of the tiny grains have coalesced to form large grains with a clear boundary. This is well characterized by the HRTEM in Fig. 3k and l. Compared with pristine Co–NiO$_x$, the lattice constant in Co–NiO$_x$@GDY increases at the interface between the GDY and the edge of the Co–NiO$_x$. Generally, the lattice constant of the (400) plane of Co–NiO$_x$ increases from 0.203 to 0.214 nm, accompanied by

the increase in the (311) plane of Co–NiO$_x$ from 0.242 to 0.248 nm. Meanwhile, the lattice constant of the (110) plane of NiO increases from 0.148 to 0.254 nm. As clearly observed in the HRTEM images (Fig. 3l), many disordered domains were formed at the interface between the GDY and Co–NiO$_x$ species after the *in situ* growth of the GDY on the Co–NiO$_x$ surface, which are beneficial for regulating the local electronic structures and coordination environments, and beneficial for improving the catalytic activity of the samples

(Supplementary Fig. S12) [49–51]. Besides, a specific characteristic crystallization pattern of the GDY with an interplanar distance of 0.465 nm can be revealed which matches that of the ABC stacking mode (Supplementary Fig. S10c). The AFM results show that the Co–NiO$_x$H$_y$ nanosheets have a thickness of ≈2.0 nm (Fig. 3m and Supplementary Fig. S13), whereas the Co–NiO$_x$ nanosheets have a thickness of ≈1.5 nm (Fig. 3n and Supplementary Fig. S14). Excitingly, after *in situ* growth of the GDY, the AFM image clearly reveals two different heights of nanosheets (Fig. 3p) and a clear step-like change in the thickness measurement represented in Fig. 3p clearly identifies the superposition of a 1.5-nm Co–NiO$_x$ layer and a 1.8-nm GDY layer.

Contact angle measurements (Fig. 4a) showed that Co–NiO$_x$@GDY has a super hydrophilic surface with a contact of 0° (Supplementary Fig. S15). Raman and XPS measurements were further performed to study the structure of the catalysts. As shown in Fig. 4b, the peak at 473 cm$^{-1}$ could be attributed to the stretching vibrations of the Co–O and Ni–O bonds in the E$_{2g}$ Raman active mode; the peaks at 519 and 616 cm$^{-1}$ can be indexed to the F$_{2g}$ and A$_{1g}$ Raman active modes of the Co–O stretching vibration of the Co–NiO$_x$ sample, respectively [52]. There are no peaks corresponding to the OH group that could be observed from the Raman spectra, indicating the complete formation of the Co–Ni oxide phase after the calcination treatment. For Co–NiO$_x$@GDY, four characteristic peaks corresponding to the D band (1385.4 cm$^{-1}$) and G band (1568.5 cm$^{-1}$) and the vibrations of the conjugated diyne links (1934.5 and 2170.3 cm$^{-1}$) were observed [53]. The magnified Raman spectra demonstrated that the signal of Co–NiO$_x$ still remains after the *in situ* growth of graphdiyne (Supplementary Fig. S16). Moreover, the XPS survey spectra for the samples (Fig. 4c) confirmed the presence of Ni, Co and O elements in Co–NiO$_x$H$_y$ and Co–NiO$_x$ while an additional C signal could be observed in Co–NiO$_x$@GDY. These results solidly confirmed the successful growth of GDY on the surface of the mixed metal oxides, indicating the successful construction of multi-heterojunction interfacial structures. The Ni 2p XPS spectra (Fig. 4d) were well fitted with two spin–orbit doublets and two shakeup satellites (denoted as 'Sat.'). For Co–NiO$_x$, the Ni 2p peaks at 854.0/871.5 and 855.9/873.5 eV are characteristic for the Ni$^{2+}$ and Ni$^{3+}$ species, respectively. The satellite peaks at ∼860.4 and ∼879.8 eV represented shakeup-type peaks of nickel at the high binding energies of Ni 2p$_{3/2}$ and Ni 2p$_{1/2}$. After the *in situ* growth of graphdiyne, the Ni species showed a slight negative shift of 0.3 eV compared with that

in Co–NiO$_x$. The ratio of Ni$^{3+}$/Ni$^{2+}$ is calculated as 0.919 for Co–NiO$_x$, while the ratio of Ni$^{3+}$/Ni$^{2+}$ is calculated as 0.810 for Co–NiO$_x$@GDY with a slight decline (Supplementary Fig. S17). The decrease in the ratio of Ni$^{3+}$/Ni$^{2+}$ is consistent with the negative shift of Ni 2p, which demonstrates the electron-withdrawing property of Ni species in the catalyst. The Co 2p XPS spectrum (Fig. 4e) was also fitted with two spin–orbit doublets and two shakeup satellites at ∼802.8 and ∼786.5 eV. For Co–NiO$_x$, the binding energies at 779.5 and 794.7 eV can be ascribed to Co$^{3+}$ species and the others at 781.2 and 796.6 eV were ascribed to Co$^{2+}$ species. After the *in situ* growth of graphdiyne, the Co species showed a slight positive shift of 0.2 eV compared with that in Co–NiO$_x$. In addition, for Co–NiO$_x$, the ratio of Co$^{3+}$/Co$^{2+}$ is calculated as 1.559 while the ratio of Co$^{3+}$/Co$^{2}$ is calculated as 1.396 for Co–NiO$_x$@GDY with a slight decline (Supplementary Fig. S18). The decrease in the ratio of Co$^{3+}$/Co$^{2}$ is consistent with the result that the positive shift of Co 2p, which demonstrates the electron-withdrawing property of Co species in the catalyst. The above-discussed XPS results demonstrate that the Co, Ni species in the catalyst possess mixed valence states, which has been demonstrated to enhance the catalytic activity. The O 1s XPS spectra (Fig. 4f) for Co–NiO$_x$ showed two peaks of metal–O (529.2 eV) and adsorbed oxygen (530.8 eV). For Co–NiO$_x$@GDY, the newly formed peak at 532.4 eV could be ascribed to the C–O bonds between the O elements in Co–NiO$_x$ and the C elements in GDY. This also indicate the formation of the 'C–O–metal' structures at the heterointerfaces between Co–NiO$_x$ and GDY, which benefits the formation of new catalytic active sites [54]. As shown in Fig. 4g, four sub-peaks corresponding to the C–C (sp$^2$, 283.9 eV), C–C (sp, 284.9 eV), C–O (286.3 eV) and C=O (288.2 eV) were observed for pristine GDY. For Co–NiO$_x$@GDY, in addition to the characteristic peaks for C–C (sp$^2$, 283.9 eV), C–C (sp, 285.2 eV), C–O (286.4 eV) and C=O (288.4 eV), an additional $\pi$–$\pi^*$ satellite peak at 289.95 eV was observed, indicating the interactions between GDY and Co–NiO$_x$ species. The intensity ratio of C–C (sp$^2$) to C–C(sp) for Co–NiO$_x$@GDY remains at 0.5, demonstrating the successful growth of GDY on the Co–NiO$_x$ surface. The positive shifts in the binding energies in the sp–C peak indicate the electron-donating property of GDY. These results demonstrated the successful construction of the heterojunction interfacial donor–acceptor structures with incomplete electron transfer between Co–NiO$_x$ species and GDY. Moreover, the presence of mixed nickel–cobalt oxidation states in Co–NiO$_x$@GDY also can promote the electron
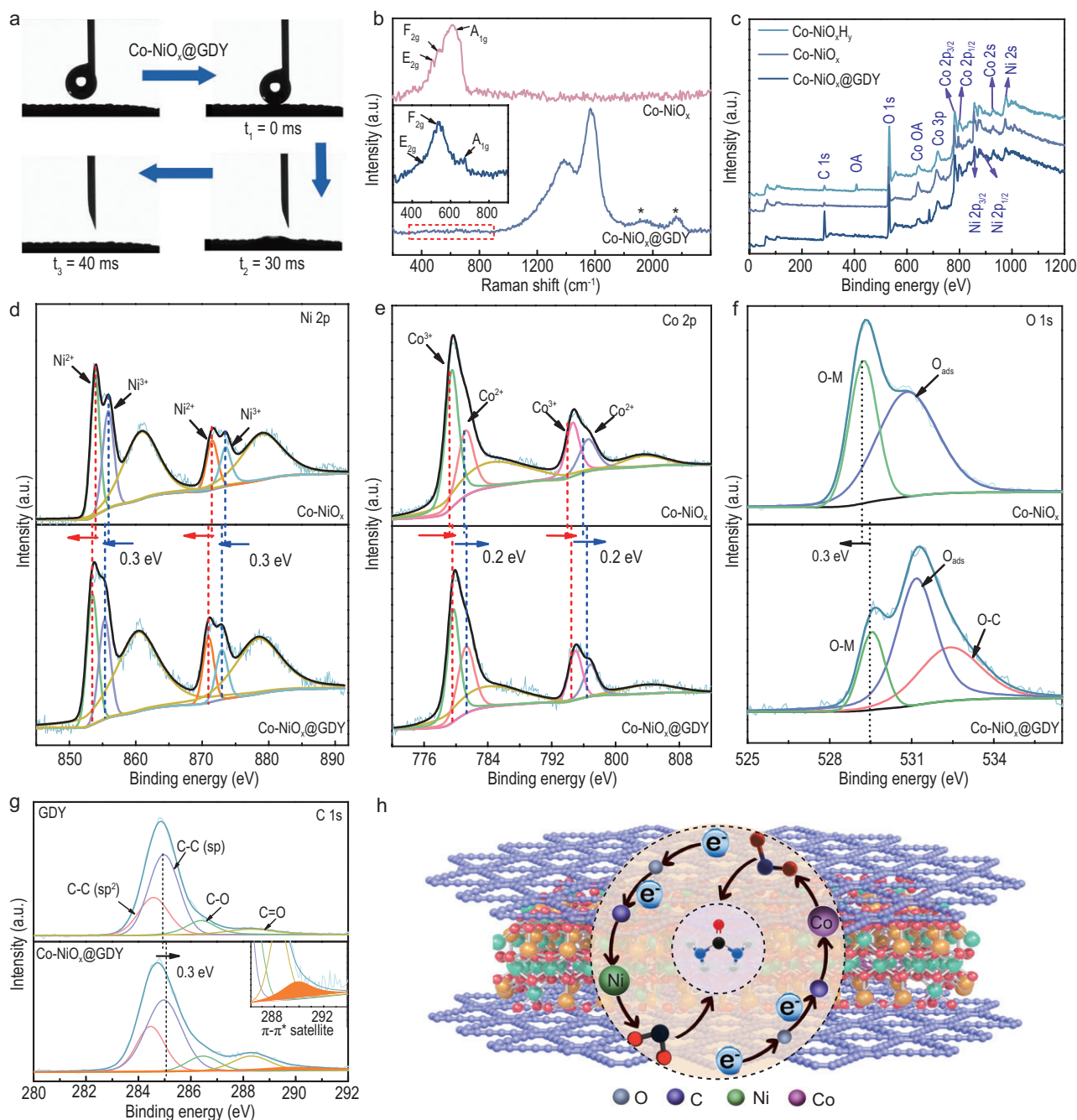
**Figure 4.** (a) Contact angle measurements of Co–NiO$_x$@GDY. (b) Raman spectra of Co–NiO$_x$ and Co–NiO$_x$@GDY. (c) XPS survey spectra of Co–NiO$_x$H$_y$, Co–NiO$_x$ and Co–NiO$_x$@GDY samples. The high-resolution (d) Ni 2p, (e) Co 2p and (f) O 1s XPS spectra of Co–NiO$_x$ and Co–NiO$_x$@GDY, respectively. (g) The high-resolution C 1s XPS spectra of GDY and Co–NiO$_x$@GDY. Inset in (g): the $\pi - \pi^*$ transition peak of Co–NiO$_x$@GDY. (h) Schematic representation of the charge transfer of the multi-heterojunction interfacial structure.

transfer between Co–NiO$_x$ and GDY, leading to great enhancement in the catalytic ability [55–57].

The electrocatalytic performance of the as-synthesized catalysts toward urea production was studied in an H-type electrolytic cell at ambient temperatures and pressures (Supplementary Fig. S19). CO$_2$ gas continuously flowed into the cathodic electrolyte containing 0.01 M NaNO$_2$. The

concentration of the produced urea was measured using the diacetyl monoxime method (Supplementary information). Figure 5a reveals that the onset potential of Co–NiO$_x$@GDY is much more positive and the current density is higher than that of pristine Co–NiO$_x$. Co–NiO$_x$@GDY with optimized contents of 3.51 wt% achieved the maximum FE value of 64.3% (Supplementary Fig. S20 and Supplementary
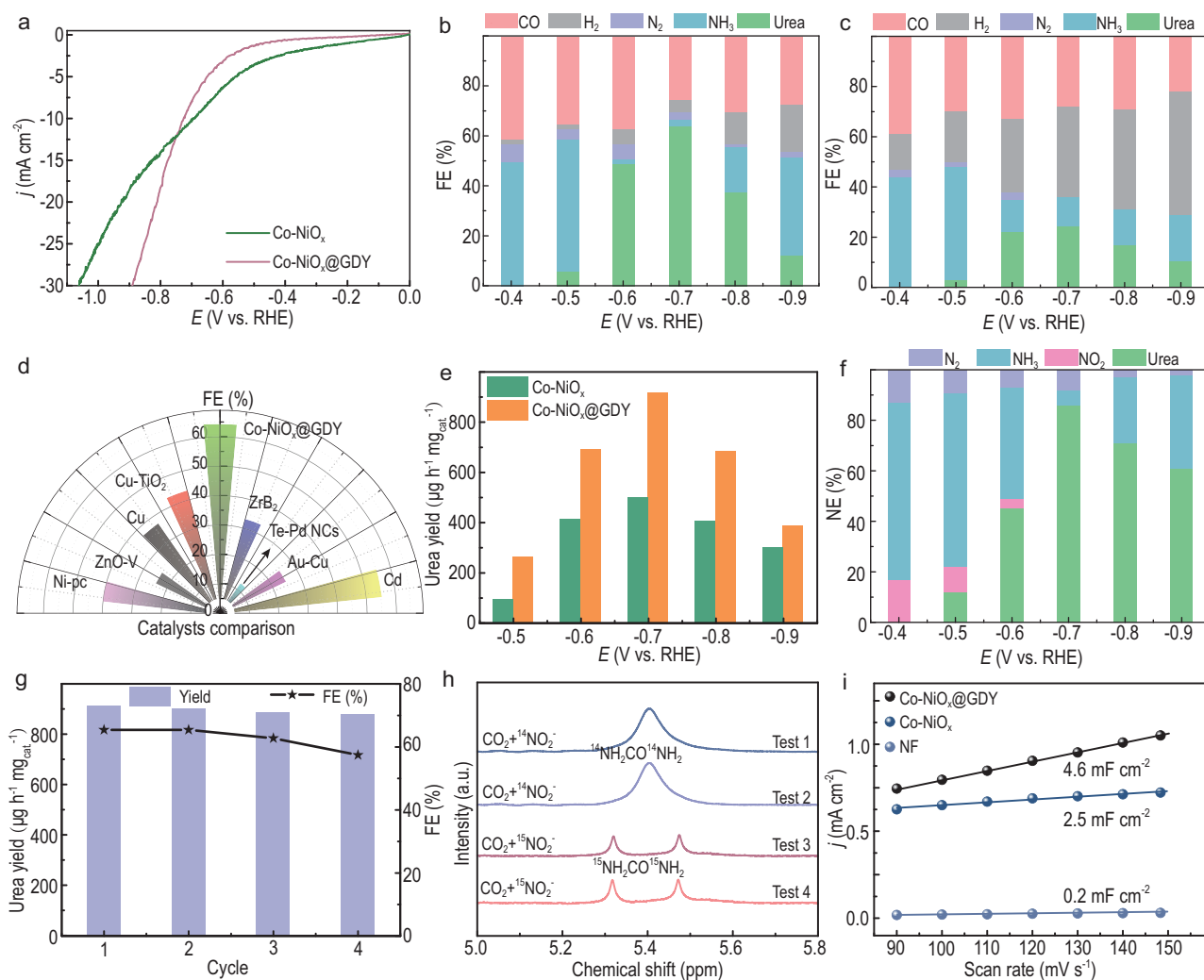
**Figure 5.** (a) Linear sweep voltammetry curves for Co–NiO$_x$ and Co–NiO$_x$@GDY in CO$_2$-saturated 0.01 M NaNO$_2$ solution at a scan rate of 2 mV s$^{-1}$. FE obtained at different potentials for (b) Co–NiO$_x$@GDY and (c) Co–NiO$_x$. (d) Comparison of the FE value of Co–NiO$_x$@GDY with reported catalysts. (e) Urea yield rates of Co–NiO$_x$ and Co–NiO$_x$@GDY obtained at different potentials. (f) N$_{urea}$-selectivity at different potentials for Co–NiO$_x$@GDY. (g) Stability tests for continuous generation of urea. (h) $^1$H NMR spectra of the electrolyte obtained in $^{15}$N-Isotope labeling experiments. (i) The capacitive currents plotted against the scan rates from 90 to 150 mV s$^{-1}$.

Table S1) at a low applied potential of $-0.7$ V versus RHE (Fig. 5b), which is almost three times higher than that of Co–NiO$_x$ at 24.3% (Fig. 5c and Supplementary Fig. S21) and 15 times higher than that of pure GDY at 4.42% (Supplementary Fig. S22) and much higher than all reported electrocatalysts, such as Ni–Pc (40%) [58], Cu–TiO$_2$ (43.1%) [59], Te–Pd NCs (12.2%) [19] and ZnO–V (23.3%) [60] (Fig. 5d). It is worth mentioning that the electrolyte concentration is optimized for maximum FE (Supplementary Fig. S23). It was observed that the FE for urea production decreased with the further increase in the applied potentials, which might be due to the interference of the side reactions. In order to determine the specific role of each part in the electrocatalysts in promoting urea synthesis, samples of

NiO, CoO, Co–NiO$_x$, NiO@GDY and CoO@GDY were prepared (Supplementary Fig. S24). The catalytic performances of these samples have also been measured in urea synthesis (Fig. 5e and Supplementary Fig. S25). Co–NiO$_x$@GDY shows the best catalytic performance with the highest FE (64.3%) and urea yield rates (Y$_{urea}$, 913.2 $\mu$g h$^{-1}$ mg$_{cat}^{-1}$) compared with that of NiO (FE = 6.6%; Y$_{urea}$ = 221.9 $\mu$g h$^{-1}$ mg$_{cat}^{-1}$), CoO (FE = 14.3%; Y$_{urea}$ = 217.9 $\mu$g h$^{-1}$ mg$_{cat}^{-1}$), Co–NiO$_x$ (FE = 24.3%; Y$_{urea}$ = 497.2 $\mu$g h$^{-1}$ mg$_{cat}^{-1}$), NiO@GDY (FE = 16%; Y$_{urea}$ = 221.9 $\mu$g h$^{-1}$ mg$_{cat}^{-1}$) and CoO@GDY (FE = 20.4%; Y$_{urea}$ = 356.3 $\mu$g h$^{-1}$ mg$_{cat}^{-1}$). It was found that the catalytic performances of the samples with multiple components were better than

those with single components, which might be due to the formation of mixed valence states of the metal species and the grain boundary dislocations in the multicomponent sample. Besides, the introduction of GDY can greatly improve the catalytic activity of the samples due to the formation of strong incomplete charge transfer between GDY and the metal atoms at the multi-heterojunction interface, which can significantly improve the conductivity, increase the number of active sites and finally enhance the overall electrocatalytic performances of the electrocatalyst for urea synthesis. Based on above discussion, the strong incomplete charge transfer between the GDY and metal oxide interface that occurred on the multi-heterojunction interface structure of the electrocatalyst plays a critical role in enhancing the catalytic performance for urea synthesis. Interestingly, the amounts of CO during the urea production process in nitrite-containing electrolytes were obviously lower than those absent of nitrite at all potentials (Supplementary Fig. S26), which indicates that the resulted $_*$CO from $CO_2$ reduction mainly participates in the C–N coupling reaction forming urea and simultaneously inhibits the parallel competition reactions, which can greatly increase the FE of the reaction. In order to precisely determine the distribution of N species during the urea production process, the NE results were calculated (Fig. 5f). When compared to the electrolyte without $CO_2$, the conversion of $NO_2^-$ and the production of $NH_3$ are increased in $CO_2$-saturated electrolytes (Supplementary Fig. S27). Co–$NiO_x$@GDY shows the maximum urea NE of 86.2% at −0.7 V versus RHE, which indicates that almost all of the produced $NH_3$ species were used as the reactants for urea production. The FE and $Y_{urea}$ of Co–$NiO_x$@GDY remained almost unchanged before and after the stability test (Fig. 5g). Besides, detailed characterizations (e.g. SEM, TEM and EDX mapping measurements) on Co–$NiO_x$@GDY obtained after long-time urea electrosynthesis showed no obvious changes in morphology and composition during the reaction, indicating the excellent stability of the catalyst (Supplementary Figs S28–S30). The isotopic labeling tests (Fig. 5h) using $^{15}NO_2^-$ as the N-source solidly demonstrated that the nitrogen in the synthesized urea originated from the nitrite in the electrolytes. The double-layer capacitance of Co–$NiO_x$@GDY was 4.6 mF $cm^{-2}$, which is larger than that of Co–$NiO_x$ (2.5 mF $cm^{-2}$) and the pure Ni foam (0.2 mF $cm^{-2}$) (Fig. 5i and Supplementary Figs S31–S33), revealing the largest electrochemically active surface area and further indicating the ideally engineered interface structure between Co–$NiO_x$ and GDY with the best conductivity, the most facilitated charge-transfer

kinetics, possessing essential advantages for efficient catalysis.

In order to validate the C–N coupling mechanism of Co–$NiO_x$@GDY, advanced operando SR-FTIR measurements were further carried out (Fig. 6a). Figure 6b shows the typical FTIR spectrum of the GDY in which the peaks at 2122 and 2210 $cm^{-1}$ originate from the typical C≡C stretching vibration. The same peaks of our Co–$NiO_x$@GDY indicate the successful fabrication of the multi-heterointerface structure. The peak at 3568 $cm^{-1}$ (Fig. 6c) indicates the $CO_2$ adsorption on the catalysts and the peaks at 3440 and 3390 $cm^{-1}$ indicate the formation of N–H during the reaction. The peak at 1670 $cm^{-1}$ (Fig. 6d and e) is assigned to the stretching of C=O and the peak at 1625 $cm^{-1}$ is assigned to the O–H hydrogen bonding that seems to be due to the change in the adsorption configuration of water molecules after increasing the potential. Additionally, the peaks at 1578 and 1163 $cm^{-1}$ belong to the bending mode and rocking mode of N–H, which indicates the formation of $_*NH_2$. And the peaks at 1419 and 1396 $cm^{-1}$ reveal the presence of C–N and OCO, respectively [61–63]. An additional series of enhanced peaks at 1363 $cm^{-1}$ represents the dissociated N=O obtained after adsorption on the Co–$NiO_x$@GDY with increasing potential. The faint peak that appeared at 1200 $cm^{-1}$ represents the adsorption of the intermediate $_*CO_2NH_2$ with the hydroxyl. Compared with free urea, the shift in the stretching frequency for C–N implies that the produced urea interacted at the Co–$NiO_x$@GDY surface via the O atoms in C=O. The overall urea electrosynthesis of the process involves four steps. First, the oxygen atoms in the nitrite electrolyte connect with the oxygen vacancy in Co–$NiO_x$@GDY; second, the multi-step protons-couple occurs with the corresponding electron transfer to further form the important $NH_{2*}$ intermediate. Next, the $CO_2$ molecules fill the vacancies in the Co–$NiO_x$@GDY and are transferred to the $COOH_*$ intermediate through a proton-coupled electron-transfer process; ultimately, the urea is formed by $_*CO_2NH_2$ intermediates coupled from the $NH_{2*}$ and $COOH_*$ (Fig. 6f) [64].

## CONCLUSIONS

Continuous synthesis of urea products under ambient conditions has not yet been realized by science and technology at present. Our study explored a sustainable urea production route using nitrite, carbon dioxide and water, and achieved high-performance synthesis under ambient conditions. Selective and active urea production with a record-high FE of
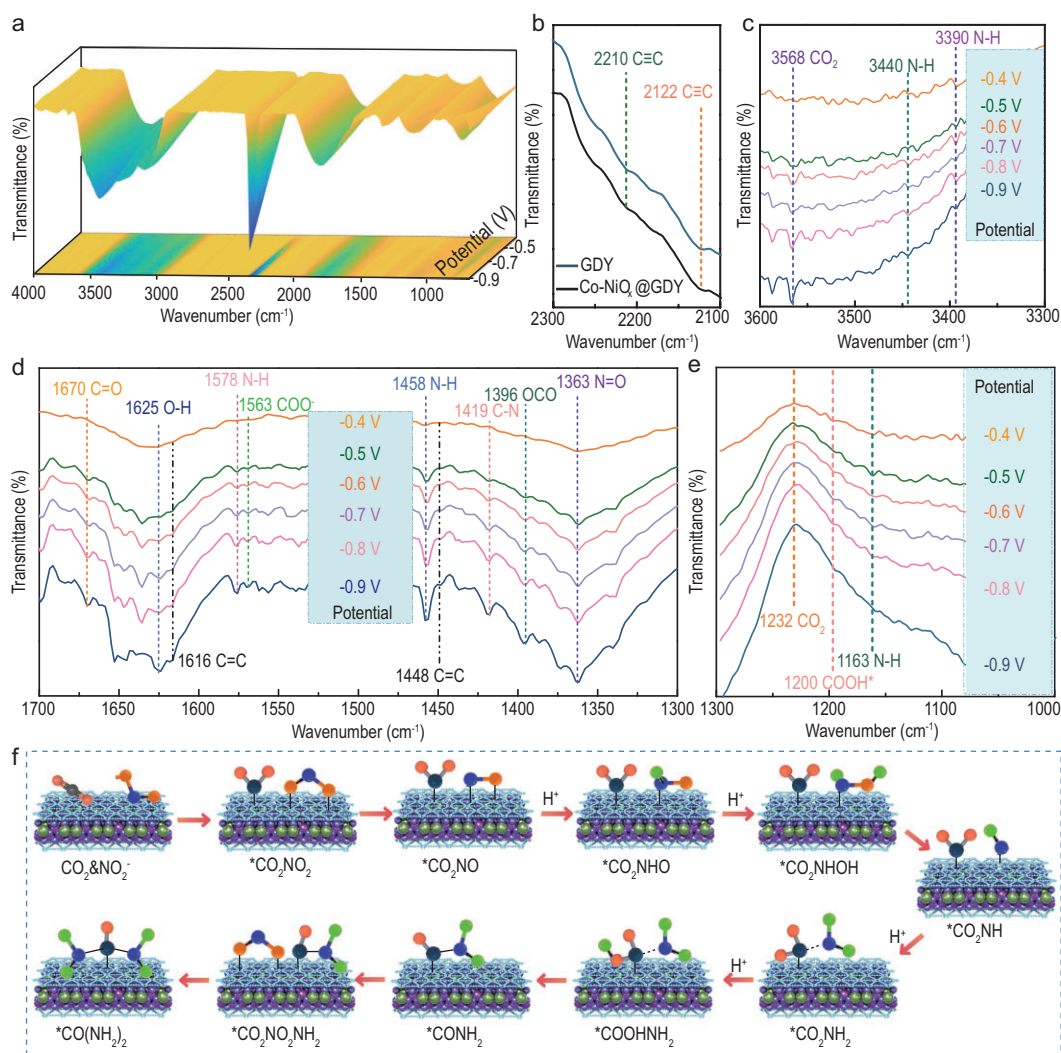
**Figure 6.** Operando SR-FTIR spectroscopy measurements under various potentials for Co–NiO$_x$@GDY during electrocatalytic coupling of nitrate and carbon dioxide. (a) Three-dimensional FTIR spectra in the range of 4000–700 cm$^{-1}$. (b) Experimental FTIR spectrum of GDY. (c) Infrared signals in the range of 3600–3300 cm$^{-1}$. (d) Infrared signals in the range of 1700–1300 cm$^{-1}$. (e) Infrared signals in the range of 1300–1000 cm$^{-1}$. (f) Reaction mechanism studies for electrocatalytic urea synthesis on Co–NiO$_x$@GDY.

64.3%, N$_{urea}$-selectivity of 86.0%, C$_{urea}$-selectivity of ∼100%, urea yield rates of 913.2 $\mu$g h$^{-1}$ mg$_{cat}$$^{-1}$ and excellent long-term stability on Co–NiO$_x$@GDY was realized. Experimental results demonstrate that the *in situ* grown multi-heterojunction interfacial structure could lead to the formation of the strong incomplete charge-transfer phenomenon between a GDY and metal oxide interface and multiple intermolecular interactions. These effectively optimize the intermediate's adsorption/desorption abilities and promote direct C–N coupling by significantly suppressing by-product reactions toward the formation of H$_2$, CO, N$_2$ and NH$_3$. Operando SR-FTIR results reveal the C–N coupling mechanism for urea synthesis. This work provides new insights into the design and synthesis of a multi-heterointerface

catalyst for highly selective and efficient C–N coupling originating from NO$_2$$^-$ and CO$_2$ under ambient conditions, which is a step forward towards the development of large-scale electrolysers.

## SUPPLEMENTARY DATA

Supplementary data are available at *NSR* online.

## FUNDING

## AUTHOR CONTRIBUTIONS

Y.L. supervised the research. Y.X. and Y.L. conceived the idea and designed the experiments. D.Z. conducted the material preparations, the material characterization, electrochemical measurements and the data analysis. X.Z. and C.Z. helped with the electrochemical tests. All authors contributed to the discussion of the data.

*Conflict of interest statement.* None declared.

## REFERENCES

1. Erisman JW, Sutton MA and Galloway J *et al.* How a century of ammonia synthesis changed the world. *Nat Geosci* 2008; **1**: 636–9.
2. Service RF. New recipe produces ammonia from air, water, and sunlight. *Science* 2014; **345**: 610.
3. Scattolin T, Bouayad-Gervais S and Schoenebeck F. Straightforward access to N-trifluoromethyl amides, carbamates, thiocarbamates and ureas. *Nature* 2019; **573**: 102–7.
4. Geng S-K, Zheng Y and Li S-Q *et al.* Nickel ferrocyanide as a high-performance urea oxidation electrocatalyst. *Nat Energy* 2021; **6**: 904–12.
5. Chen J-G, Crooks RM and Seefeldt LC *et al.* Beyond fossil fuel-driven nitrogen transformations. *Science* 2018; **360**: eaar6611.
6. Chen C, He N and Wang S. Electrocatalytic C–N coupling for urea synthesis. *Small Sci* 2021; **1**: 2100070.
7. Hao Y-C, Guo Y and Chen L-W *et al.* Promoting nitrogen electroreduction to ammonia with bismuth nanocrystals and potassium cations in water. *Nat Catal* 2019; **2**: 448–56.
8. Liang J, Chen H and Mou T *et al.* Coupling denitrification and ammonia synthesis via selective electrochemical reduction of nitric oxide over $Fe_2O_3$ nanorods. *J Mater Chem A* 2022; **10**: 6454–62.
9. Lv P, Wu D and He B *et al.* An efficient screening strategy towards multifunctional catalysts for the simultaneous electroreduction of $NO_3^-$, $NO_2^-$ and NO to $NH_3$. *J Mater Chem A* 2022; **10**: 9707–16.
10. Foster SL, Bakovic SIP and Duda RD *et al.* Catalysts for nitrogen reduction to ammonia. *Nat Catal* 2018; **1**: 490–500.
11. Licht S, Cui B and Wang B *et al.* Ammonia synthesis by $N_2$ and steam electrolysis in molten hydroxide suspensions of nanoscale $Fe_2O_3$. *Science* 2014; **345**: 637–40.
12. Wang J, Yu L and Hu L *et al.* Ambient ammonia synthesis via palladium-catalyzed electrohydrogenation of dinitrogen at low overpotential. *Nat Commun* 2018; **9**: 1795.
13. Li Y, Lu X-F and Xi S *et al.* Synthesis of N-Doped highly graphitic carbon urchin-like hollow structures loaded with single-ni atoms towards efficient $CO_2$ electroreduction. *Angew Chem Int Ed* 2022; **61**: e202201491.
14. Yu X, Han P and Wei Z *et al.* Boron-doped graphene for electrocatalytic $N_2$ reduction. *Joule* 2018; **2**: 1610–22.
15. Zhang X, Davidson EA and Mauzerall DL *et al.* Managing nitrogen for sustainable development. *Nature* 2015; **528**: 51–9.
16. Chen C, Zhu X and Wen X *et al.* Coupling $N_2$ and $CO_2$ in $H_2O$ to synthesize urea under ambient conditions. *Nat Chem* 2020; **12**: 717–24.
17. Yuan M, Chen J and Bai Y *et al.* Unveiling electrochemical urea synthesis by co-activation of $CO_2$ and $N_2$ with Mott–Schottky heterostructure catalysts. *Angew Chem* 2021; **133**: 11005–13.
18. van der Ham CJ, Koper MT and Hetterscheid DG. Challenges in reduction of dinitrogen by proton and electron transfer. *Chem Soc Rev* 2014; **43**: 5183–91.
19. Feng Y, Yang H and Zhang Y *et al.* Te-doped Pd nanocrystal for electrochemical urea production by efficiently coupling carbon dioxide reduction with nitrite reduction. *Nano Lett* 2020; **20**: 8282–9.
20. Jouny M, Lv J-J and Cheng T *et al.* Formation of carbon–nitrogen bonds in carbon monoxide electrolysis. *Nat Chem* 2019; **11**: 846–51.
21. Peng J, Sun H and Ni K *et al.* Hierarchical palladium catalyst for highly active and stable water oxidation in acidic media. *Natl Sci Rev* 2022; **9**: nwac108.
22. van Deelen TW, Hernández Mejía C and de Jong KP. Control of metal-support interactions in heterogeneous catalysts to enhance activity and selectivity. *Nat Catal* 2019; **2**: 955–70.
23. Zhu D-D, Liu J-L and Qiao S-Z. Recent advances in inorganic heterogeneous electrocatalysts for reduction of carbon dioxide. *Adv Mater* 2016; **28**: 3423–52.
24. Lu X-F, Fang Y and Luan D *et al.* Metal–organic frameworks derived functional materials for electrochemical energy storage and conversion: a mini review. *Nano Lett* 2021; **21**: 1555–65.
25. Li X, Liu L and Ren X *et al.* Microenvironment modulation of single-atom catalysts and their roles in electrochemical energy conversion. *Sci Adv* 2020; **6**: eabb6833.
26. Wu C-H, Liu C and Su D *et al.* Bimetallic synergy in cobalt–palladium nanocatalysts for CO oxidation. *Nat Catal* 2019; **2**: 78–85.
27. Zecevic J, Vanbutsele G and de Jong KP *et al.* Nanoscale intimacy in bifunctional catalysts for selective conversion of hydrocarbons. *Nature* 2015; **528**: 245–8.
28. Cheng W, Zhao X and Su H *et al.* Lattice-strained metal–organic-framework arrays for bifunctional oxygen electrocatalysis. *Nat Energy* 2019; **4**: 115–22.
29. Farmer JA and Campbell CT. Ceria maintains smaller metal catalyst particles by strong metal-support bonding. *Science* 2010; **329**: 933–6.
30. Li D, Xu F and Tang X *et al.* Induced activation of the commercial $Cu/ZnO/Al_2O_3$ catalyst for the steam reforming of methanol. *Nat Catal* 2022; **5**: 99–108.
31. Pu T, Shen L and Liu X *et al.* Formation and influence of surface hydroxyls on product selectivity during $CO_2$ hydrogenation by $Ni/SiO_2$ catalysts. *J Catal* 2021; **400**: 228–33.
32. Li G, Li Y and Liu H *et al.* Architecture of graphdiyne nanoscale films. *Chem Commun* 2010; **46**: 3256–8.
33. Fang Y, Liu Y and Qi L *et al.* 2D graphdiyne: an emerging carbon material. *Chem Soc Rev* 2022; **51**: 2681–709.
34. Li Y, Xu L and Liu H *et al.* Graphdiyne and graphyne: from theoretical predictions to practical construction. *Chem Soc Rev* 2014; **43**: 2572–86.
35. Xue Y, Li Y and Zhang J *et al.* 2D graphdiyne materials: challenges and opportunities in energy field. *Sci China Chem* 2018; **61**: 765–86.

36. Fang Y, Xue Y and Li Y *et al.* Graphdiyne interface engineering: highly active and selective ammonia synthesis. *Angew Chem* 2020; **132**: 13121–7.

37. Gao Y, Xue Y and He F *et al.* Controlled growth of a high selectivity interface for seawater electrolysis. *Proc Natl Acad Sci USA* 2022; **119**: e2206946119.

38. Du Y, Zhou W and Gao J *et al.* Fundament and application of graphdiyne in electrochemical energy. *Acc Chem Res* 2020; **53**: 459–69.

39. Xue Y, Huang B and Yi Y *et al.* Anchoring zero valence single atoms of nickel and iron on graphdiyne for hydrogen evolution. *Nat Commun* 2018; **9**: 1460.

40. Gao X, Liu H and Wang D *et al.* Graphdiyne: synthesis, properties, and applications. *Chem Soc Rev* 2019; **48**: 908–36.

41. Mason JA, McDonald TM and Bae TH *et al.* Application of a high-throughput analyzer in evaluating solid adsorbents for post-combustion carbon capture via multicomponent adsorption of $CO_2$, $N_2$, and $H_2O$. *J Am Chem Soc* 2015; **137**: 4787–803.

42. Wang S, Li Y and Dai S *et al.* Prediction by convolutional neural networks of $CO_2/N_2$ selectivity in porous carbons from $N_2$ adsorption isotherm at 77 K. *Angew Chem* 2020; **132**: 19813–6.

43. Ma F-X, Yu L and Xu C-Y *et al.* Self-supported formation of hierarchical $NiCo_2O_4$ tetragonal microtubes with enhanced electrochemical properties. *Energy Environ Sci* 2016; **9**: 862–6.

44. Pang Y, Li J and Wang Z *et al.* Efficient electrocatalytic conversion of carbon monoxide to propanol using fragmented copper. *Nat Catal* 2019; **2**: 251–8.

45. Huang P-Y, Ruiz-Vargas CS and van der Zande AM *et al.* Grains and grain boundaries in single-layer graphene atomic patchwork quilts. *Nature* 2011; **469**: 389–92.

46. Kim C J, Brown L and Graham M W *et al.* Stacking order dependent second harmonic generation and topological defects in h-BN bilayers. *Nano Lett* 2013; **13**: 5660–5.

47. van der Zande AM, Huang PY and Chenet DA *et al.* Grains and grain boundaries in highly crystalline monolayer molybdenum disulphide. *Nat Mater* 2013; **12**: 554–61.

48. Ye C, Liu J and Zhang Q *et al.* Activating metal oxides nanocatalysts for electrocatalytic water oxidation by quenching-induced near-surface metal atom functionality. *J Am Chem Soc* 2021; **143**: 14169–77.

49. Yan D, Li Y and Huo J *et al.* Defect chemistry of nonprecious-metal electrocatalysts for oxygen reactions. *Adv Mater* 2017; **29**: 1606459.

50. Zhu Q, Pan Z and Zhao Z *et al.* Defect-driven selective metal oxidation at atomic scale. *Nat Commun* 2021; **12**: 558.

51. Gao C, Wang J and Xu H *et al.* Coordination chemistry in the design of heterogeneous photocatalysts. *Chem Soc Rev* 2017; **46**: 2799–823.

52. Chen L, Yang J and Klaus S *et al.* p-Type transparent conducting oxide/n-type semiconductor heterojunctions for efficient and stable solar water oxidation. *J Am Chem Soc* 2015; **137**: 9595–603.

53. Fang Y, Xue Y and Hui L *et al.* Graphdiyne@Janus magnetite for photocatalytic nitrogen fixation. *Angew Chem* 2021; **133**: 3207–11.

54. Yao Y, Zhu Y and Pan C *et al.* Interfacial sp C–O–Mo hybridization originated high-current density hydrogen evolution. *J Am Chem Soc* 2021; **143**: 8720–30.

55. Huang Z-F, Song J and Du Y *et al.* Chemical and structural origin of lattice oxygen oxidation in Co–Zn oxyhydroxide oxygen evolution electrocatalysts. *Nat Energy* 2019; **4**: 329–38.

56. Kang J, Qiu X and Hu Q *et al.* Valence oscillation and dynamic active sites in monolayer NiCo hydroxides for water oxidation. *Nat Catal* 2021; **4**: 1050–8.

57. He Z, Hwang J and Gong Z *et al.* Promoting biomass electrooxidation via modulating proton and oxygen anion deintercalation in hydroxide. *Nat Commun* 2022; **13**: 3777.

58. Shibata M and Furuya N. Electrochemical synthesis of urea at gas-diffusion electrodes: Part VI: simultaneous reduction of carbon dioxide and nitrite ions with various metallophthalocyanine catalysts. *J Electroanal Chem* 2001; **507**: 177–84.

59. Cao N, Quan Y and Guan A *et al.* Oxygen vacancies enhanced cooperative electrocatalytic reduction of carbon dioxide and nitrite ions to urea. *J Colloid Interface Sci* 2020; **577**: 109–14.

60. Meng N, Huang Y and Liu Y *et al.* Electrosynthesis of urea from nitrite and $CO_2$ over oxygen vacancy-rich ZnO porous nanosheets. *Cell Rep Phys Sci* 2021; **2**: 100378.

61. Sun C and Xue D. IR spectral study of mesoscale process during urea crystallization from aqueous solution. *Cryst Growth Des* 2015; **15**: 2867–73.

62. Yue D, Jia Y and Yao Y *et al.* Structure and electrochemical behavior of ionic liquid analogue based on choline chloride and urea. *Electrochim Acta* 2012; **65**: 30–6.

63. Yao Y, Zhu S and Wang H *et al.* A spectroscopic study on the nitrogen electrochemical reduction reaction on gold and platinum surfaces. *J Am Chem Soc* 2018; **140**: 1496–501.

64. Huang Y, Yang R and Wang C *et al.* Direct electrosynthesis of urea from carbon dioxide and nitric oxide. *ACS Energy Lett* 2022; **7**: 284–91.